

Crystal field splittings and magnetic ground state of the square-lattice antiferromagnets $\text{YbBi}_2\text{ClO}_4$ and YbBi_2IO_4 with $J_{\text{eff}} = 1/2^*$

Pyeongjae Park,^{1,†} Qianli Ma,² G. Sala,³ S. Calder,² Douglas L. Abernathy,²
Matthew B. Stone,² Andrew F. May,¹ and Andrew D. Christianson^{1,‡}

¹*Materials Science & Technology Division, Oak Ridge National Laboratory, Oak Ridge, Tennessee 37831, USA*

²*Neutron Scattering Division, Oak Ridge National Laboratory, Oak Ridge, Tennessee 37831, USA*

³*Oak Ridge National Laboratory, Oak Ridge, TN, 37831, USA*

We report on the crystal field level splitting and magnetic ground state of the $J_{\text{eff}} = 1/2$ square lattice antiferromagnets $\text{YbBi}_2\text{ClO}_4$ and YbBi_2IO_4 using powder inelastic neutron scattering (INS) and neutron diffraction measurements. Both compounds exhibit a well-isolated Γ_7 doublet ground state under a tetragonal crystal field environment, confirming a robust $J_{\text{eff}} = 1/2$ picture with slight XY-type anisotropic character in the g -tensor. Notably, the ground state wave functions closely resemble the Γ_7 doublet expected in the perfect cubic limit, consistent with the nearly cubic ligand configuration of eight O^{2-} ions surrounding Yb^{3+} . Below $T_N = 0.21$ K, YbBi_2IO_4 exhibits a stripe long-range magnetic order characterized by an ordering wave vector $\mathbf{q}_m = (1/2, 0, 0)$ or its symmetry-equivalent $(0, 1/2, 0)$, with magnetic moments aligned along \mathbf{q}_m . The ordered moment is approximately 79% of the classical prediction, significantly larger than expected from the isotropic $J_1 - J_2$ model, suggesting the possible involvement of exchange anisotropy in explaining this observation. We show that symmetry-allowed XXZ and bond-dependent anisotropic exchange terms in a square lattice can play a critical role in stabilizing the stripe order and suppressing the moment reduction as observed. These findings establish $\text{YbBi}_2\text{ClO}_4$ and YbBi_2IO_4 as unique platforms for exploring rich $J_{\text{eff}} = 1/2$ magnetism from two less investigated perspectives: (i) on a square lattice and (ii) within a (nearly) cubic ligand environment.

I. INTRODUCTION

The $S = 1/2$ square lattice antiferromagnet (SqAF) serves as a textbook model in the study of low-dimensional quantum magnetism [1–5]. The Heisenberg model with isotropic nearest-neighbor (NN) and second NN antiferromagnetic interactions (the $J_1 - J_2$ model) has been extensively studied for its potential to manifest a quantum spin liquid state (QSL) [6–9]. The ratio J_2/J_1 indicates the degree of additional quantum fluctuations induced by exchange frustration, which are maximized at $J_2 = 0.5J_1$. Theoretical studies have shown that a QSL can emerge in the range $0.4 < J_2/J_1 < 0.6$, separating regions of two well-known magnetic orders: Néel-type ($J_2/J_1 < 0.4$) and stripe-type ($J_2/J_1 > 0.6$) [6–9]. Notably, this phase diagram is very similar to that of the $J_1 - J_2$ Heisenberg model for $S = 1/2$ triangular lattice systems [10–12].

A compelling extension to these isotropic quantum spin models is exploring the effect of exchange anisotropy

on quantum fluctuations. Such anisotropies can involve Ising- or planar-type XXZ anisotropies [13–16], and more intriguingly, symmetry-allowed bond-dependent anisotropy terms [17–21], each of which capable of introducing unique magnetic properties. A key factor in the recent success of investigations on exchange anisotropy is the effective spin-1/2 degree of freedom in isolated Kramers doublet ground states ($J_{\text{eff}} = 1/2$), where the intrinsic coupling between spin and orbital degrees of freedom enables significant exchange anisotropy [22]. However, experimental studies of $J_{\text{eff}} = 1/2$ square lattice materials with exchange anisotropy have remained lacking, limiting insights into the anisotropic spin model in $S = 1/2$ SqAFs.

YbBi_2IO_4 and $\text{YbBi}_2\text{ClO}_4$ have recently been suggested as nearly ideal realizations of a 2D $J_{\text{eff}} = 1/2$ square lattice antiferromagnet [23, 24]. These compounds crystallize in a tetragonal structure ($P4/mmm$ space group), with Yb^{3+} ions forming layered square lattices [Fig. 1(a)] [23, 25]. Each Yb^{3+} ion is surrounded by a nearly cubic configuration of oxygen ligands with a marginal tetragonal distortion [$d_{ab}/d_c = 0.996$, see Fig. 1(b)] [23]. The $J_{\text{eff}} = 1/2$ nature of the Yb^{3+} ions was inferred from heat capacity measurements, which revealed a total magnetic entropy of $R \ln(2)$ [23, 24]. Temperature-dependent magnetic susceptibility [$\chi(T)$] of both compounds exhibits a broad maximum at a temperature $T_{\text{max}} = 0.33$ K (0.38 K) in YbBi_2IO_4 ($\text{YbBi}_2\text{ClO}_4$), indicating the quasi-2D nature of their magnetic Hamiltonian [23]. While Ref. [23] reported the onset of 3D long-range order below $T_N = 0.21$ K (0.25 K) in YbBi_2IO_4 ($\text{YbBi}_2\text{ClO}_4$) based on a sharp lambda-like feature in $C(T)$, Ref. [24] presented a qualitatively different $C(T)$

* This manuscript has been authored by UT-Battelle, LLC under Contract No. DE-AC05-00OR22725 with the U.S. Department of Energy. The United States Government retains and the publisher, by accepting the article for publication, acknowledges that the United States Government retains a non-exclusive, paid-up, irrevocable, world-wide license to publish or reproduce the published form of this manuscript, or allow others to do so, for United States Government purposes. The Department of Energy will provide public access to these results of federally sponsored research in accordance with the DOE Public Access Plan (<http://energy.gov/downloads/doe-public-access-plan>).

† parkp@ornl.gov

‡ christiansad@ornl.gov

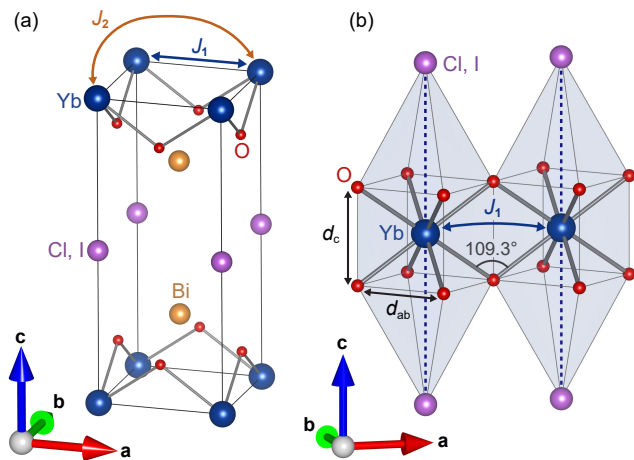


FIG. 1. Crystal structure of $\text{YbBi}_2(\text{Cl, I})\text{O}_4$. (a) The tetragonal unit cell of $\text{YbBi}_2(\text{Cl, I})\text{O}_4$ [space group $P4/mmm$ ($\#123$)]. The Yb ions form a stack of square lattices well separated by Bi and Cl (I) layers. (b) The oxygen coordination of the Yb ions. The distances between Yb and O are all equal. The ratio of in-plane to out-of-plane O–O distances (d_{ab}/d_c) are 0.996 for both $\text{YbBi}_2\text{ClO}_4$ and YbBi_2IO_4 [23]. This tiny elongation results in a Yb–O–Yb bond angle of 109.3° , nearly identical to the ideal tetrahedral angle of $\cos^{-1}(-1/3) = 109.47^\circ$. Crystal structures were drawn with Vesta [30].

curve and suggested the absence of long-range order. Most importantly, the presence of a sizable J_2 was inferred from the much larger Curie-Weiss temperature magnitude ($|\theta_{CW}|$) compared to T_{\max} , i.e., magnetic frustration, [23]. A quantitative estimation of J_2/J_1 using high-temperature series expansion analysis of the isotropic J_1 - J_2 model, assuming $J_1 > J_2$, resulted in J_2/J_1 close to 0.27 in these two compounds [23], within the Néel ordered phase.

These bulk properties strongly motivate further investigation into the microscopic magnetism of YbBi_2IO_4 and $\text{YbBi}_2\text{ClO}_4$, particularly regarding their spin Hamiltonians and associated quantum fluctuations. Notably, the simple theoretical analysis described above assumes an isotropic spin model, whereas the possibility of anisotropic exchange interactions between NNs should also be considered as potentially important in $J_{\text{eff}} = 1/2$ systems with edge-sharing ligand environments. Interestingly, YbBi_2IO_4 and $\text{YbBi}_2\text{ClO}_4$ feature a cubic-like configuration of O_4^{2-} ligands, entirely different from the octahedral ligand configurations that have been extensively studied [17, 19, 22, 26–29]. This unique environment provides an opportunity to explore $J_{\text{eff}} = 1/2$ magnetism under entirely different conditions, potentially offering new insights into spin-orbital coupled interactions.

In this article, we present inelastic neutron scattering (INS) and neutron diffraction measurements of $\text{YbBi}_2\text{ClO}_4$ and YbBi_2IO_4 , which reveal the crystal field splittings of Yb^{3+} ions and the long-range order of the $J_{\text{eff}} = 1/2$ magnetic moments in YbBi_2IO_4 . The crystal

field levels measured by INS confirm that Yb^{3+} exhibits a Kramers doublet ground state separated by about 80 meV from the first excited states in both $\text{YbBi}_2\text{ClO}_4$ and YbBi_2IO_4 , supporting the picture of $J_{\text{eff}} = 1/2$ square-lattice magnetism at the magnetic energy scale (~ 1 K). The crystal field Hamiltonian and the corresponding ground state wave function were derived by fitting the energy and dynamical structure factors of the measured excitations. This reveals a Γ_7 doublet ground state not far from the perfect cubic limit but exhibits slight XY-type anisotropy in their g -tensor. Powder neutron diffraction measurements of YbBi_2IO_4 at dilution refrigerator temperatures reveal magnetic Bragg peaks corresponding to an ordering wave vector $\mathbf{q}_m = (1/2, 0, 0)$ or its symmetry-equivalent directions, indicating a stripe magnetic order, antithetical to the proposed order based upon high temperature susceptibility measurements. Rietveld refinement shows that the magnetic moments point along \mathbf{q}_m , with a magnitude 79% of the classical prediction without quantum fluctuations. We discuss a spin model and corresponding degree of quantum fluctuations for YbBi_2IO_4 and $\text{YbBi}_2\text{ClO}_4$ compatible with these findings, suggesting that these compounds may host sizable exchange anisotropy beyond the isotropic $J_1 - J_2$ model.

II. EXPERIMENTAL DETAILS

Polycrystalline $\text{YbBi}_2\text{ClO}_4$ and YbBi_2IO_4 were prepared by solid-state reaction as described in Ref. [23]. $\text{LuBi}_2\text{ClO}_4$ and LuBi_2IO_4 , the nonmagnetic analogs of $\text{YbBi}_2\text{ClO}_4$ and YbBi_2IO_4 , were synthesized by similar methods using reactions at 950°C for 100 h followed by grinding and an additional heating step at 900°C for 100 h. The Lu-based compounds are used in the INS measurements to quantify the extent of the signal due to phonon scattering.

INS measurements of the crystal field splitting were performed with the ARCS spectrometer at the Spallation Neutron Source at the Oak Ridge National Laboratory (ORNL). Samples were loaded in aluminum (Al) sample cans with 1 atmosphere of helium gas. Data were collected using an incident energy of $E_i = 160$ meV, with the Fermi chopper set to 600 Hz, providing an energy resolution of ≈ 6.1 meV (full-width at half-maximum) at the elastic line. Background signals were estimated by measurements of nonmagnetic analogs $\text{LuBi}_2\text{ClO}_4$ and LuBi_2IO_4 under the same temperature, using identical Al sample cans. Empty can measurements were subtracted from all datasets unless otherwise noted. Data processing was carried out using the Dave [31] and Mantid [32] software packages.

Powder neutron diffraction measurements of YbBi_2IO_4 were conducted with the HB-2A powder diffractometer at the High Flux Isotope Reactor at ORNL. To access temperatures below $T_N = 0.21$ K, we used a dilution refrigerator. Approximately 9 g of poly-

crystalline YbBi_2IO_4 were loaded into a standard copper sample can. The can was filled with over-pressurized helium gas ($p = 10$ atm), which was necessary to ensure the sample fully thermalized at temperatures below T_N . Data were collected using a wavelength of 2.41 \AA at temperatures of 0.04 K , 0.25 K , and 1.5 K , with a counting time of approximately 8 hours per temperature. We used the FullProf software package to perform Rietveld refinement of crystal and magnetic structures [33].

III. RESULTS

A. Crystal field level splitting

Yb^{3+} , a Kramers ion, has a $J = 7/2$ multiplet ground state ($^2F_{7/2}$ in term symbol formalism) that can split into a maximum of four Kramers doublets. In $\text{YbBi}_2\text{ClO}_4$ and YbBi_2IO_4 , Yb^{3+} ions lie in a tetragonal environment coordinated by eight oxygen ions and two I or Cl ions [Fig. 1(b)], with the $4/mmm$ site symmetry. This configuration results in four Kramers doublets and therefore should have three excited levels.

Our powder INS measurements successfully identified these three excited crystal field levels in $\text{YbBi}_2\text{ClO}_4$ and YbBi_2IO_4 . Figures 2(a)–(b) show the powder INS spectra of $\text{YbBi}_2\text{ClO}_4$ and YbBi_2IO_4 at 10 K with an incident neutron energy of 160 meV . Three clear, flat excitations are observed in both compounds as indicated by red arrows in Figs. 2(a)–(b). They exhibit higher intensity in the low-momentum ($|\mathbf{Q}|$) region indicating the behavior of a magnetic form factor, and are absent in the INS spectra of the nonmagnetic analogs $\text{LuBi}_2\text{ClO}_4$ and LuBi_2IO_4 . These observations confirm that the excitation signals correspond to Yb^{3+} crystal field levels.

Notably, all excited levels are located above 79 meV in both compounds, indicating that the ground-state Kramers doublet is well isolated at temperatures comparable to the magnetic energy scale ($\sim 1 \text{ K}$) of $\text{YbBi}_2\text{ClO}_4$ and YbBi_2IO_4 . This ensures an exact $J_{\text{eff}} = 1/2$ picture, consistent with prior magnetic entropy measurements showing saturation at $R \ln(2)$ [23]. In addition, no noticeable difference is observed between the spectra collected at 10 K and 100 K , as the activation energy ($\sim 80 \text{ meV}$) still dominates over the thermal fluctuation energy at 100 K .

The eigenvalues and relative dynamical structure factors of the three excited levels were analyzed quantitatively using constant wave-vector scans through the crystal field excitation spectra (integrated over the momentum range $4 < |\mathbf{Q}| < 5 \text{ \AA}^{-1}$), as shown in Figs. 3(a) and 3(e). These values were obtained by simultaneously fitting the three peaks with Lorentzian profiles, in which we refined the amplitude (= structure factors), center position (= eigenvalues), linewidth, and a global constant background. A multiplicative scaling factor was applied to the overall intensity during the fit.

The resultant eigenvalues and structure factor ratios,

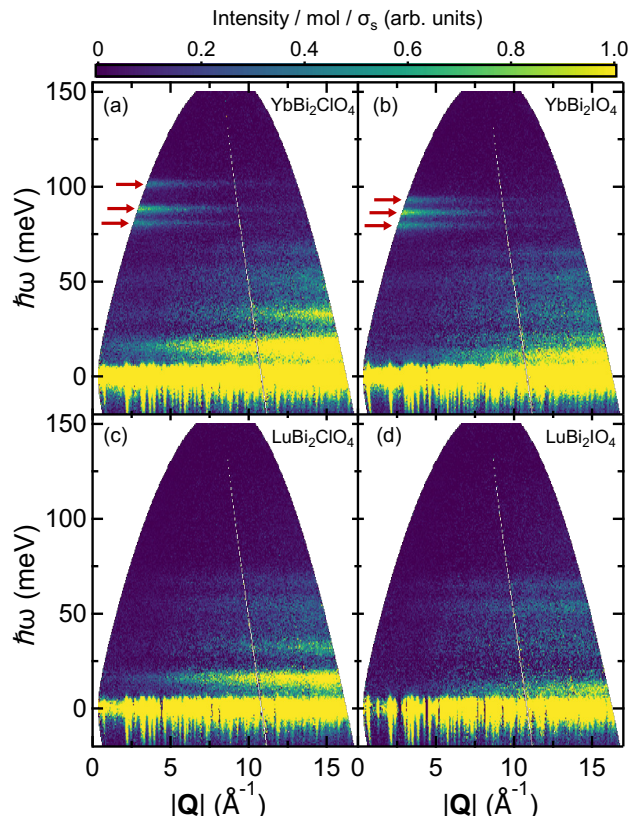


FIG. 2. INS intensity measured at $T = 10 \text{ K}$ as a function of energy ($\hbar\omega$) and wave-vector transfer ($|\mathbf{Q}|$) for (a) $\text{YbBi}_2\text{ClO}_4$, (b) YbBi_2IO_4 , (c) $\text{LuBi}_2\text{ClO}_4$, and (d) LuBi_2IO_4 . Data were acquired using the ARCS instrument as detailed in the text. The intensity has been normalized to the product of the number of measured moles of the sample and the total scattering cross-section per formula unit. Data have had an empty can background subtraction applied prior to normalization. All data are shown on the same intensity scale. Red arrows indicate the three excited crystal field levels of Yb^{3+} in these materials.

TABLE I. Fitted eigenvalues ($\hbar\omega_i, i = 1, 2, 3$) and relative spectral weights (I_i/I_j) of the three crystal field excitations in for $\text{YbBi}_2\text{ClO}_4$ and YbBi_2IO_4 .

	$\text{YbBi}_2\text{ClO}_4$	YbBi_2IO_4
$\hbar\omega_1$ (meV)	80.78	79.61
$\hbar\omega_2$ (meV)	88.12	86.32
$\hbar\omega_3$ (meV)	101.31	92.65
I_1/I_2	0.560	0.756
I_3/I_2	0.591	0.469

summarized in Table I, provide crucial information of the tetragonal crystal field Hamiltonian and corresponding eigenstates of each compound. With the c -axis as the unique tetragonal axis [see Fig. 1(b)], the crystal field

Hamiltonian (\hat{H}_{CF}) can be expressed as [34, 35]:

$$\hat{H}_{\text{CF}} = B_2^0 \hat{O}_2^0 + B_4^0 \hat{O}_4^0 + B_4^4 \hat{O}_4^4 + B_6^0 \hat{O}_6^0 + B_6^4 \hat{O}_6^4, \quad (1)$$

where \hat{O}_n^m are conventional Stevens operators [36], and B_n^m are the corresponding crystal field parameters. This Hamiltonian yields the following four doublet states represented by two 2D irreducible representations, Γ_7^t and Γ_6^t [35]:

$$\begin{aligned} |\Gamma_{7,1}^t\rangle &= \pm c_1 |\pm \frac{5}{2}\rangle \pm c_2 |\mp \frac{3}{2}\rangle, \\ |\Gamma_{7,2}^t\rangle &= \mp c_1 |\pm \frac{5}{2}\rangle \pm c_2 |\mp \frac{3}{2}\rangle, \\ |\Gamma_{6,1}^t\rangle &= \pm a_1 |\mp \frac{7}{2}\rangle \pm a_2 |\pm \frac{1}{2}\rangle, \\ |\Gamma_{6,2}^t\rangle &= \mp a_1 |\mp \frac{7}{2}\rangle \pm a_2 |\pm \frac{1}{2}\rangle, \end{aligned} \quad (2)$$

where M_J in $|M_J\rangle \equiv |J = 7/2, M_J\rangle$ denotes the eigenvalue of \hat{J}_z , and the normalized coefficients $c_{1,2}$ and $a_{1,2}$ depend on B_n^m .

While determining B_n^m is typically achieved by minimizing the χ^2 metric between the observed and calculated crystal field spectra, this approach could potentially end up with multiple possible solutions. To ensure physically meaningful results based on sufficient constraints, we simultaneously fit the crystal field spectrum and the temperature-dependent magnetic susceptibility. This was performed by minimizing a custom-defined loss function using CrysFieldExplorer [37]:

$$L_{\text{tot}} = L_{\text{Spectrum}} + L_{1/\chi}, \quad (3)$$

where L_{Spectrum} and $L_{1/\chi}$ are the loss functions concerning the crystal field spectra [Fig. 3(a) and 3(e)] and the inverse-susceptibility [Fig. 3(b) and 3(f)], respectively. L_{Spectrum} is further defined as $L_E + L_{\text{Intensity}}$. Their explicit functional expressions are:

$$L_E = \log_{10} \left(\sum_i^n \det\{(E_{\text{exp}}[i] + E_{\text{cal}}[0])\mathbf{I} - H_{\text{CF}}\}^2 \right), \quad (4)$$

$$L_{\text{Intensity}} = \frac{\sqrt{\sum_i^n (I_{\text{true}}[i] - I_{\text{calc}}[i])^2}}{\sqrt{(\sum I_{\text{true}}[i])^2}}, \quad (5)$$

$$L_{1/\chi} = \frac{\sqrt{(1/\chi_{\text{exp}} - 1/\chi_{\text{calc}})^2}}{\sqrt{(1/\chi_{\text{exp}})^2}}. \quad (6)$$

where the summation runs through 1 to n -th crystal field levels of Yb^{3+} . $E_{\text{exp}}[i]$ represents the energy levels of the observed crystal field excitations determined by fitting Lorentzian convolved Gaussians to the constant wave-vector scans in Figs. 3(a) and 3(e). $E_{\text{calc}}[0]$ is eigenvalues obtained from the diagonalization of the crystal field Hamiltonian H_{CF} (Eq. (1)). \mathbf{I} is the identity matrix. $I_{\text{true}}[i]$ and $I_{\text{calc}}[i]$ are the normalized observed and calculated intensities for the i -th CEF excitation.

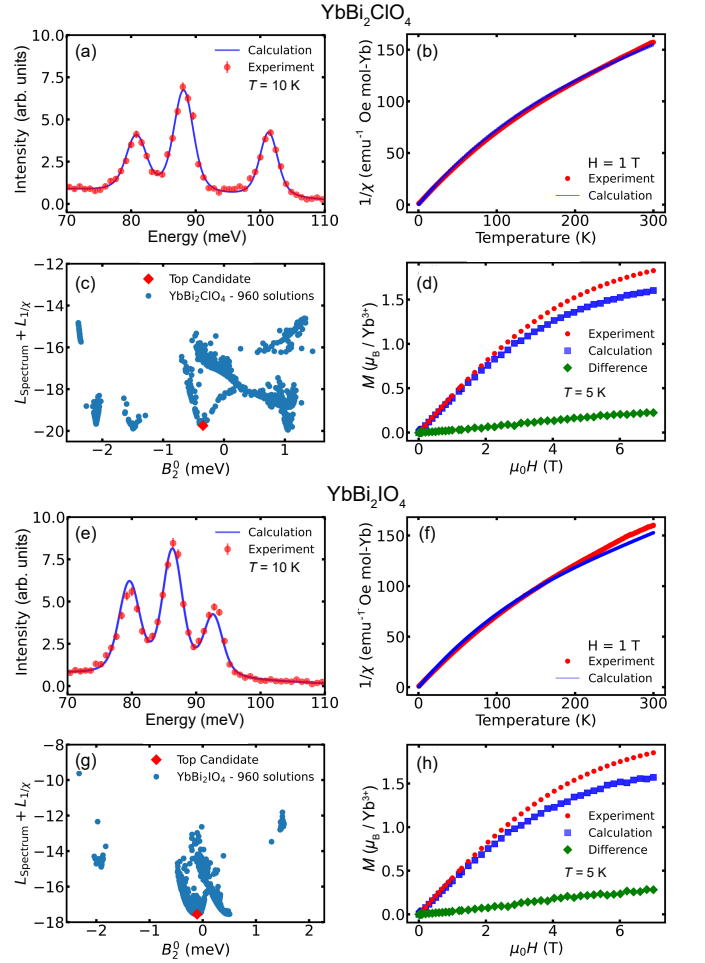


FIG. 3. Quantitative analysis of the crystal field excitations and magnetic susceptibility. (a) Energy dependence of the measured INS intensity ($4 \text{ \AA}^{-1} < |\mathbf{Q}| < 5 \text{ \AA}^{-1}$) at 10 K (red circles) from $\text{YbBi}_2\text{ClO}_4$. The solid blue line represents the calculated INS cross-section based on the best-fitted crystal field parameters B_n^m from TABLE. II. The line spans from and to the energy transfer range included in the fit. (b) Measured and calculated inverse magnetic susceptibility for $\text{YbBi}_2\text{ClO}_4$, with the latter derived from the model in TABLE. II. (c) Five-dimensional goodness-of-fit landscape for the $\text{YbBi}_2\text{ClO}_4$ Hamiltonian, projected onto the B_0^2 axis. The red diamond marks the solution presented in TABLE. II. (d) Comparison of the measured and calculated field-dependent magnetization at 5 K. (e)–(h) Same as (a)–(d), but for YbBi_2IO_4 . Simulations in (e)–(h) are based on the solution with $B_0^2 = -0.107 \text{ meV}$ (see TABLE II).

χ_{exp} and χ_{calc} denotes the experimentally measured and calculated magnetic susceptibility data. Details of the construction of the loss functions are demonstrated in Ref. [37].

The results of minimizing L_{tot} throughout the five-dimensional parameter space are shown in Fig. 3(c) and Fig. 3(g). The key term in Eq. (1) concerning the tetragonal nature of $\text{YbBi}_2\text{ClO}_4$ and YbBi_2IO_4 is $B_2^0 \hat{O}_2^0$. The other four terms are also allowed under cubic symmetry.

TABLE II. The optimized Stevens operator coefficients (B_n^m) for $\text{YbBi}_2\text{ClO}_4$ and YbBi_2IO_4 , and corresponding wave function coefficients and g -factors. The uncertainty in the fitted B_n^m values is approximately 4% of their value; see the main text. For YbBi_2IO_4 , two viable solutions are presented, both of which exhibit nearly identical ground state wave functions, making them equivalent from the $J_{\text{eff}} = 1/2$ magnetism perspective. In all cases, the four doublets in Eq. (3) are arranged in ascending energy order as $\Gamma_{7,1}^t - \Gamma_{6,1}^t - \Gamma_{7,2}^t - \Gamma_{6,2}^t$ (also see Appendix A). The d_{ab}/d_c values are adapted from Ref. [23].

	$\text{YbBi}_2\text{ClO}_4$	YbBi_2IO_4	YbBi_2IO_4
B_2^0 (meV)	-0.3441	-0.1068	0.4870
B_4^0 (meV)	0.0496	0.0433	0.0421
B_4^4 (meV)	0.2740	0.2862	0.2780
B_6^0 (meV)	-0.0003	-0.0004	0.0001
B_6^4 (meV)	-0.018	-0.0168	-0.0179
c_1	-0.8143	-0.7851	-0.7868
c_2	0.5804	0.6194	0.6172
a_1	-0.9999	-0.9820	-0.052
a_2	0.0080	0.1890	-0.9986
Ground state	$ \Gamma_{7,1}^t\rangle$	$ \Gamma_{7,1}^t\rangle$	$ \Gamma_{7,1}^t\rangle$
g_{ab}	3.74	3.85	3.85
g_c	2.63	2.21	2.23
d_{ab}/d_c	0.996	0.996	0.996

Given the importance of B_2^0 , we minimized L_{tot} for a fixed B_2^0 value, repeating this process across a range of $-2.5 \text{ meV} < B_2^0 < 1.5 \text{ meV}$.

For $\text{YbBi}_2\text{ClO}_4$, good fits were achieved by three solutions at $B_2^0 = -1.48, -0.344$, and 1.06 meV , as shown in Fig. 3(c) as a deep local minimum of the L_{tot} landscape. However, a careful analysis of their resultant ground states reveals that the cases of $B_2^0 = -1.48$ and 1.06 meV exhibit unphysical features inconsistent with bulk characterization results, which is described in Appendix A. For YbBi_2IO_4 , we found two potential solutions at $B_2^0 = -0.107$ and 0.487 meV [Fig. 3(g)], but further analysis could not conclusively distinguish between these solutions, as described below.

The full parameter set for each solution and the corresponding wave functions are summarized in TABLE II, along with their coefficients $c_{1,2}$ and $a_{1,2}$. The uncertainty in the fitted B_n^m values is estimated to be approximately 4% of their magnitude, as such variations did not produce any noticeable visual disparity in our fit results (Fig. 3). Notably, except for B_2^0 , the fitted B_n^m values are very similar across all solutions, remaining nearly within the aforementioned uncertainty range. Indeed, the corresponding ground state doublet of each solution ($|\Gamma_{7,1}^t\rangle$) is close to each other, with coefficients c_1 and c_2 differing only slightly. This consistency aligns with previous findings that YbBi_2IO_4 and $\text{YbBi}_2\text{ClO}_4$ show nearly the

same magnetic properties [23]. The corresponding in-plane (g_{ab}) and out-of-plane (g_c) g -factors of the ground state doublet, also listed in TABLE II, show a consistent profile across all solutions: $g_{\text{ab}} > g_c$, confirming an XY-like anisotropic character of the single-ion Yb^{3+} magnetism in both YbBi_2IO_4 and $\text{YbBi}_2\text{ClO}_4$.

Another noteworthy observation is that the two excited doublets, $|\Gamma_6^t\rangle$, are nearly pure $|\pm\frac{1}{2}\rangle$ or $|\pm\frac{7}{2}\rangle$ states, with minimal superposition between them. The key difference between the two solutions for YbBi_2IO_4 in TABLE II lies in the energy hierarchy of $|\pm\frac{1}{2}\rangle$ and $|\pm\frac{7}{2}\rangle$. Each solution assigns the observed excitations at $\hbar\omega_1$ and $\hbar\omega_3$ as either $|\frac{1}{2}\rangle$ and $|\frac{7}{2}\rangle$ or $|\frac{7}{2}\rangle$ and $|\frac{1}{2}\rangle$. While the data at hand cannot resolve which assignment is correct, we emphasize that both solutions yield identical magnetic properties due to their quantitatively identical ground state wave functions. The first excited level—either $|\pm\frac{1}{2}\rangle$ or $|\pm\frac{7}{2}\rangle$ —is significantly separated from the ground state and would not affect the magnetic properties at temperatures comparable to the magnetic energy scale ($\sim 1 \text{ K}$).

Of further interest is the comparison between the observed $M - H$ curves in the paramagnetic regime ($T \gg |\theta_{\text{CW}}|$) and the predictions from the fitted ground state doublet [Fig. 3(d) and 3(h)]. While the experimental curves are qualitatively consistent with theoretical expectations, showing saturation around $1.67\mu_{\text{B}}/\text{Yb}^{3+}$ (with an averaged g -factor of $(2g_{\text{ab}} + g_c)/3 \sim 3.34$ for both compounds), we found apparent underestimation of magnetization values by the calculation in the high-field regime. The origin of this discrepancy remains unclear, but notably the deviation scales linearly with field strength.

Finally, it is useful to compare our results to the case of perfect cubic symmetry, characterized by the constraints $B_2^0 = 0$, $B_4^4 = 5B_4^0$, and $B_6^4 = -21B_6^0$. In the limit $|B_4^0| \gg |B_6^0|$ (see TABLE II), this symmetry yields the following Γ_7 doublet ground state [35, 38]:

$$|\Gamma_7^c\rangle = \frac{\sqrt{3}}{2} |\pm\frac{5}{2}\rangle - \frac{1}{2} |\mp\frac{3}{2}\rangle. \quad (7)$$

This state is not far from the ground states found in YbBi_2IO_4 and $\text{YbBi}_2\text{ClO}_4$, with the fitted c_1 and c_2 coefficients showing a slight deviation from the cubic limit. Thus, despite the presence of the tetragonal characteristics, such as anisotropic g -factors, to some extent YbBi_2IO_4 and $\text{YbBi}_2\text{ClO}_4$ would retain the essence of $J_{\text{eff}} = 1/2$ magnetism typical of perfect cubic ligand environments. This aspect might be relevant to the nearly cubic arrangement of the eight oxygen anions surrounding Yb^{3+} [Fig. 1(b)], as evident in the near-unity ratio of in-plane to out-of-plane O–O distances (see TABLE I) [23].

Thus, YbBi_2IO_4 and $\text{YbBi}_2\text{ClO}_4$ offer a rare platform for studying $J_{\text{eff}} = 1/2$ magnetism in an edge-sharing (nearly) cubic environment. We note that, the magnitude of B_2^0 in TABLE II, which is the largest or second largest among the coefficients, should not be misinterpreted as it is the dominant term in the Hamiltonian. This is because, the contribution of higher order terms

in Eq. 1 accompanies a few order-of-magnitude larger multiplication factor to B_m^n in the solution and thus actually dominates over the lower order terms when their B_m^n coefficients are comparable [35]. This becomes evident when examining the analytic form of, for instance, the phase factor ϕ_7 , which is directly related to the wave function through $c_1 = \cos(\phi_7/2)$ [35]:

$$\tan \phi_7 = -\frac{2}{\sqrt{3}} \left(\frac{-15B_4^4 + 105B_6^4}{B_2^0 - 50B_4^0 - 1470B_6^0} \right). \quad (8)$$

We note that the definition of B_m^n used in this work [Eq. (1)] is different from that in Ref. [35] by constant multiplication factors.

B. Magnetic structure

The magnetic long-range order in YbBi_2IO_4 was investigated using powder neutron diffraction with a dilution refrigerator. The crystal structure of YbBi_2IO_4 has previously been studied via Rietveld refinement of time-of-flight neutron diffraction profiles collected at $T = 30\text{ K}$ [23]. We conducted the same analysis on new data collected at $T = 1.5\text{ K}$, still far above T_N [Fig. 4(a)]. The refinement result is nearly identical to that reported in our previous work [23], with no significant differences observed.

Neutron diffraction measurements at 40 mK, well below T_N , revealed the emergence of magnetic Bragg peaks in YbBi_2IO_4 [Fig. 4(b)], demonstrating the onset of long-range order. This diffraction profile corresponds to a magnetic ordering wave vector $\mathbf{q}_m = (1/2, 0, 0)$ (reciprocal lattice units, r.l.u.) or its symmetry-equivalent $\mathbf{q}_m = (0, 1/2, 0)$. For clarity, we will describe our findings based on $\mathbf{q}_m = (1/2, 0, 0)$ hereafter. This ordering wave vector generates an alternating configuration of ferromagnetic spin chains, typically referred to as a stripe [6] or columnar-type magnetic order [39]. Notably, in the isotropic $S = 1/2 J_1 - J_2$ model, such a magnetic structure is expected only for $J_2/J_1 > 0.6$, which is significantly larger than the J_2/J_1 ratio predicted for YbBi_2IO_4 from high-temperature series expansion analysis [23]. Additionally, the parallel alignment between 2D square-lattice layers implies the sign of interlayer interactions: assuming additional interlayer couplings are negligible, the NN interlayer interaction is inferred to be ferromagnetic.

The direction of magnetic moments was unambiguously determined by the absence of intensity at the $(\frac{1}{2}00)$ at $2\theta = 18^\circ$ [Fig. 4(b)]. This indicates that magnetic moments are parallel to \mathbf{q}_m [i.e., along the a -axis for $\mathbf{q}_m = (1/2, 0, 0)$], as only this orientation suppresses the $(\frac{1}{2}00)$ peak by making its neutron polarization factor zero. This is evident in the comparison between our data to simulated diffraction patterns for the $\mathbf{q}_m = (1/2, 0, 0)$ magnetic structure with moments along the a , b , and c directions [black solid lines in Fig. 4(b)]. Also, the observed magnetic Bragg peak intensities are well described

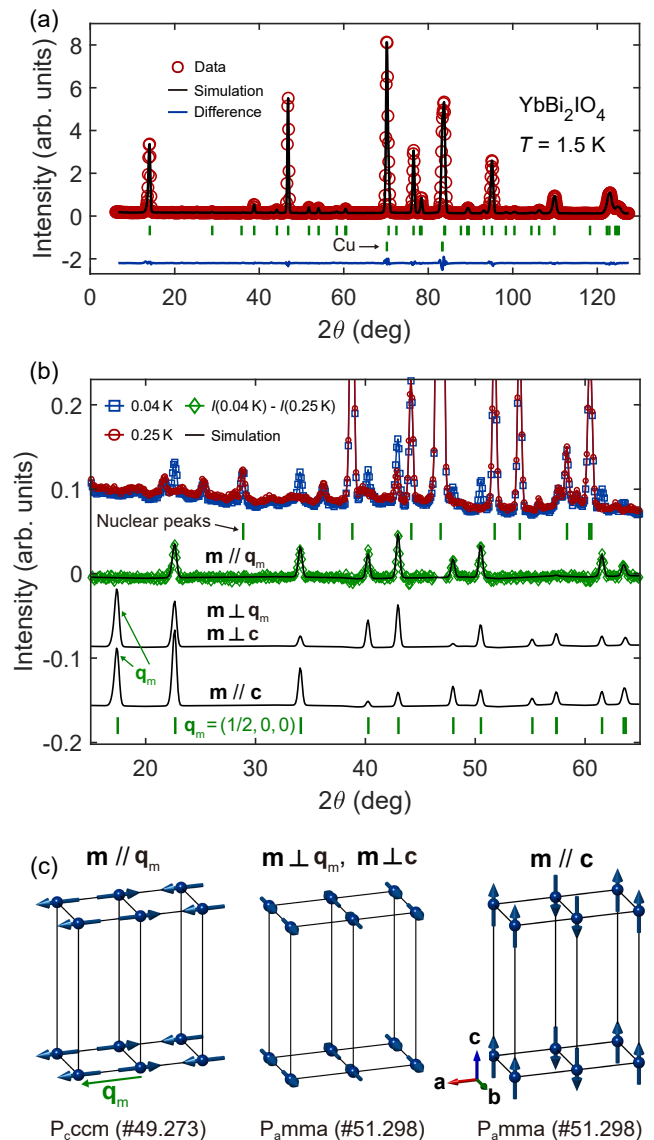


FIG. 4. Powder neutron diffraction profiles of $\text{YbBi}_2\text{ClO}_4$ and YbBi_2IO_4 collected at temperatures below and above T_N . (a) Powder diffraction pattern of YbBi_2IO_4 at $T = 1.5\text{ K}$ ($T > T_N$). (b) Magnetic diffraction profile of YbBi_2IO_4 extracted from the difference between the 0.04 K ($T < T_N$, blue-colored) and 0.25 K ($T > T_N$, red-colored) data; see green data points. Black solid lines are the three simulated diffraction patterns for magnetic moments aligned along \mathbf{q}_m , perpendicular to both \mathbf{q}_m and the c -axis, and along the c axis, respectively. (c) Three stripe magnetic structure models [with $\mathbf{q}_m = (1/2, 0, 0)$], with magnetic moments pointing along \mathbf{q}_m , perpendicular to both \mathbf{q}_m and the c -axis, and along the c -axis, respectively. The magnetic space groups (using Belov–Neronova–Smirnova notation) for each illustration are noted below.

by the model with moments parallel to \mathbf{q}_m (the a -axis). Finally, quantitative refinement of the peak intensities yields an ordered moment magnitude of $1.53(4)\mu_B/\text{Yb}^{3+}$ for YbBi_2IO_4 .

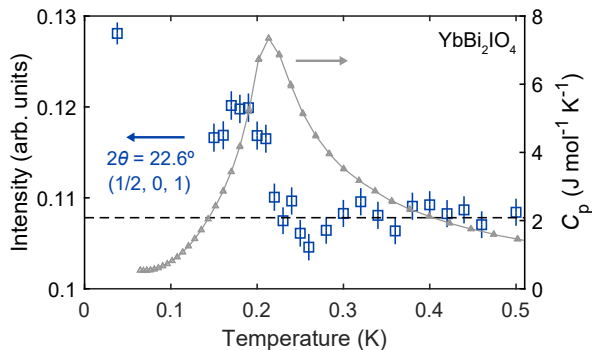


FIG. 5. Temperature dependence of the $(1/2, 0, 1)$ magnetic Bragg peak in YbBi_2IO_4 . For comparison, we overplot the temperature-dependent heat capacity of YbBi_2IO_4 [23].

Fig. 5 shows the temperature dependence of the diffraction intensity at $2\theta = 22.6^\circ$, corresponding to the $(\frac{1}{2}01)$ peak. The data reveal the emergence of the magnetic Bragg peak below around 0.21 K. This is consistent with $T_N = 0.21$ K for YbBi_2IO_4 obtained from heat capacity measurements [23], also shown in Fig. 5.

IV. DISCUSSION

The combination of crystal field splitting and the magnetic ground state presented in this work provides crucial insights concerning the nature of magnetism in $\text{YbBi}_2\text{ClO}_4$ and YbBi_2IO_4 . The observed stripe magnetic order highlights the importance of exchange interactions beyond antiferromagnetic J_1 , as the J_1 -only model predicts a Néel-type order with $\mathbf{q}_m = (1/2, 1/2, 0)$. Given the similarity in bulk properties [23] and ground state wave functions, we infer that $\text{YbBi}_2\text{ClO}_4$ likely adopts the same $\mathbf{q}_m = (1/2, 0, 0)$ ground state, although the moment direction could differ. The simplest interpretation for this observation is the presence of strong antiferromagnetic J_2 : in the isotropic $J_1 - J_2$ model, $J_2/J_1 > 0.6$ stabilizes the stripe order [6–9].

However, the isotropic $S = 1/2$ $J_1 - J_2$ model reveals limitations in describing other observations. Combining neutron diffraction ($1.53(4)\mu_B/\text{Yb}^{3+}$) with crystal field splitting analysis ($g_{ab} = 3.85$), the observed ordered moment magnitude in YbBi_2IO_4 corresponds to the 79(2)% of the classical prediction. This 21% reduction is much smaller than the 40% reduction typically expected from the isotropic $S = 1/2$ $J_1 - J_2$ model (in the absence of significant exchange frustration, i.e., $J_2 \gg J_1$ or $J_1 \gg J_2$), as confirmed by both experiment and theories [6, 40–43]. Moreover, the reduction increases further as J_2 and J_1 become more comparable since it drives the model closer to the QSL region, $0.4 < J_2/J_1 < 0.6$. While interlayer coupling (J_c) can remedy this discrepancy, a large separation between adjacent square lattice layers [Fig. 1(a)], a broad maximum in temperature-dependent magnetic susceptibility [23, 24], and preliminary estimations based

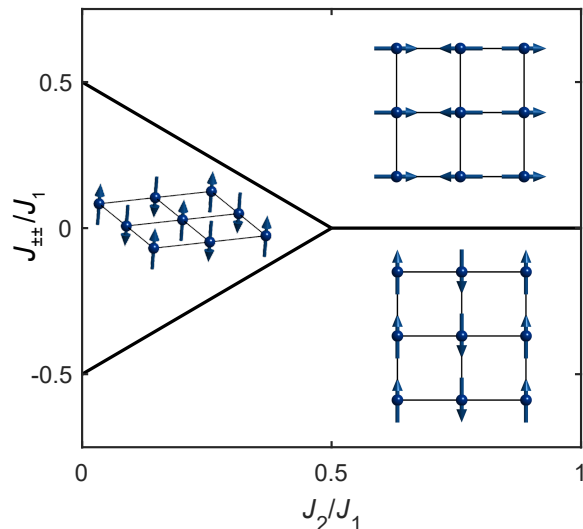


FIG. 6. Classical phase diagram of the $J_1 - J_2 - J_{\pm\pm}$ model obtained by classical Monte Carlo simulations combined with simulated annealing. For $J_{\pm\pm} = 0$, spin vectors in each phase are not fixed to the direction illustrated in the figure.

on density functional theory electronic structure [24] consistently suggest its very weak strength. Thus, incorporating J_c —likely only a few percent of J_1 or J_2 —may not suppress the moment reduction enough to the level observed [42, 44].

The above conclusion motivates us to explore the possibility of magnetic anisotropy in YbBi_2IO_4 and $\text{YbBi}_2\text{ClO}_4$. The symmetry-allowed interaction matrix between NN Yb^{3+} sites can be expressed as follows (using the parametrization notation of Δ and $J_{\pm\pm}$ commonly applied in other lattice models [20, 45]):

$$\hat{\mathcal{H}}_{ij} = \mathbf{S}_i^T \begin{pmatrix} J_1 + 2J_{\pm\pm}\tilde{c}_{ij} & 0 & 0 \\ 0 & J_1 - 2J_{\pm\pm}\tilde{c}_{ij} & 0 \\ 0 & 0 & \Delta J_1 \end{pmatrix} \mathbf{S}_j, \quad (9)$$

where \mathbf{S}_i is the (effective) spin operator acting on the localized moment at site i of a square lattice, $\tilde{c}_{ij} = \cos(2\phi_{ij})$, with ϕ_{ij} being the angle between the a-axis and the bond vector connecting sites i and j . In other words, $\tilde{c}_{ij} = \pm 1$ for the bonds along a- and b-directions, respectively.

The parameter Δ quantifies the degree of XXZ exchange anisotropy. The in-plane spin configuration found in YbBi_2IO_4 indicates that only the easy-plane type ($\Delta < 1$) is compatible. While reducing Δ from 1 does not significantly alter the phase boundaries between Néel-type and stripe magnetic orders in the isotropic $J_1 - J_2$ model, it gradually suppresses quantum fluctuations inherent to the isotropic model [43]. Notably, this behavior is very similar to the role of $\Delta < 1$ in $S = 1/2$ triangular lattice systems [13, 16, 20]. Calculations in Ref. [43] suggest that achieving a moment reduction as small as 20% roughly requires $\Delta < 0.7$, a significant level

of easy-plane anisotropy. Thus, strong easy-plane XXZ anisotropy could be one possibility of the suppressed moment reduction.

Another component, $J_{\pm\pm}$, represents bond-dependent exchange anisotropy. Notably, $J_{\pm\pm} = \pm 0.5J_1$ corresponds to the pure quantum compass model [46]. The classical phase diagram of the $J_1 - J_2 - J_{\pm\pm}$ model provides qualitative insights into the influence of $J_{\pm\pm}$ on the competition between Néel-type and stripe long-range orders (Fig. 6). Interestingly, $J_{\pm\pm}$ favors the observed stripe order over the Néel order, regardless of its sign, significantly expanding the stripe phase compared to the isotropic $J_1 - J_2$ model. We found that $J_{\pm\pm} > 0$ produces a stripe configuration consistent with our observations, where the magnetic moments align parallel to \mathbf{q}_m (Fig. 6). This makes our findings in YbBi_2IO_4 compatible with either a large $J_2/J_1 > 0$, a large $J_{\pm\pm}/J_1 > 0$, or a combination of both.

More importantly, increasing $|J_{\pm\pm}|$ is expected to gradually suppress the moment reduction in the stripe phase. In this phase, $J_{\pm\pm}$ induces an energy gap in the Goldstone mode at $\mathbf{Q} = \mathbf{q}_m$, reducing zero-point fluctuations and thereby suppressing the moment reduction. A quantitative estimation of this effect requires advanced quantum-mechanical simulations of the $J_1 - J_2 - J_{\pm\pm}$ model. Such simulations are particularly valuable for examining how the known range of the QSL phase in the isotropic model ($0.4 < J_2/J_1 < 0.6$) evolves under finite $J_{\pm\pm}$.

Given the compatibility of our observations with the two symmetry-allowed anisotropies, assessing their feasibility from a microscopic structural perspective is a crucial direction for further investigation. Numerous studies have shown that $J_{\text{eff}} = 1/2$ moments in edge-shared octahedral ligand configurations can exhibit substantial anisotropic exchange interactions, in both transition metal and rare-earth based systems [17, 19, 22, 26–29]. Since YbBi_2IO_4 and $\text{YbBi}_2\text{ClO}_4$ also feature $J_{\text{eff}} = 1/2$ moments in an edge-shared ligand environment, there is no *a priori* reason to exclude the possibility of such interactions. However, the interaction profiles strongly depend on the specific orbital arrangements of the magnetic ions and ligands. Unfortunately, theoretical studies on the cubic ligand network is still lacking. In Appendix B, we note both the important similarities and differences between octahedral and cubic ligand configurations, highlighting the challenges in drawing intuitive conclusions for cubic environments.

Experimental insights into $J_{\text{eff}} = 1/2$ magnetism in cubic ligand environments are also limited due to the scarcity of relevant materials other than YbBi_2IO_4 and $\text{YbBi}_2\text{ClO}_4$. A comparable material class is the Yb-based pyrochlore oxides $\text{Yb}_2\text{M}_2\text{O}_7$ ($M = \text{Ti, Ge, Sn}$), where Yb^{3+} is surrounded by an edge-shared polyhedron of eight oxygens [47]. Notably, INS studies on these materials revealed significant exchange anisotropy [48–50]. That being said, their oxygen configurations are substantially distorted from the ideal cubic form, limiting the

direct applicability of these findings to YbBi_2IO_4 and $\text{YbBi}_2\text{ClO}_4$.

Overall, our experimental results suggest the potential presence of exchange anisotropy in YbBi_2IO_4 (and possibly $\text{YbBi}_2\text{ClO}_4$). Determining the generalized spin Hamiltonian of these systems using cold-neutron spectroscopy is essential to unambiguously confirm this possibility. Regardless, our findings suggest that YbBi_2IO_4 and $\text{YbBi}_2\text{ClO}_4$ open a new avenue for exploring the rich $J_{\text{eff}} = 1/2$ magnetism from two perspectives: (i) on a square lattice (ii) within a nearly cubic ligand environment—both of which have been far less studied compared to the extensively investigated triangular or honeycomb systems with octahedron environments.

V. CONCLUSION

We have studied the crystal field level splitting and magnetic ground state of the $J_{\text{eff}} = 1/2$ square lattice antiferromagnets $\text{YbBi}_2\text{ClO}_4$ and YbBi_2IO_4 . Under the tetragonal crystal field environment, both compounds exhibit a well-isolated Γ_7^t doublet ground state, confirming a robust $J_{\text{eff}} = 1/2$ picture with a slight XY-type anisotropic g-tensor ($g_{ab}/g_c = 1.42$ and 1.73 in $\text{YbBi}_2\text{ClO}_4$ and YbBi_2IO_4 , respectively). The refined ground state wave functions in both compounds resemble the Γ_7^c doublet expected in the perfect cubic limit, which might be attributed to marginal tetragonal distortion [23] in the nearly cubic ligand configuration of eight O^{2-} ions. YbBi_2IO_4 exhibits a stripe long-range order below $T_N = 0.21$ K, indicating the presence of interactions beyond the isotropic J_1 . The refined ordered moment is $\sim 79\%$ of its classical prediction, considerably larger than that predicted by the isotropic $S = 1/2$ $J_1 - J_2$ model ($\sim 60\%$), which would not be fully attributed to interlayer coupling. Interestingly, symmetry-allowed XXZ and bond-dependent anisotropy terms both favor the observed magnetic structure and the suppressed moment reduction. Further investigations, including theoretical estimations of the exchange interaction profile and experimental studies using cold-neutron spectroscopy, are essential to validate the suggested anisotropic spin Hamiltonian. Our findings suggest that YbBi_2IO_4 and $\text{YbBi}_2\text{ClO}_4$ provide a rare opportunity to explore rich $J_{\text{eff}} = 1/2$ magnetism (i) on a square lattice and (ii) within a nearly cubic ligand environment.

ACKNOWLEDGMENTS

This research was supported by the U.S. Department of Energy, Office of Science, Basic Energy Sciences, Materials Science and Engineering Division. This research used resources at the High-Flux Isotope Reactor and Spallation Neutron Source, a DOE Office of Science User Facility operated by the Oak Ridge National Laboratory.

The beam time was allocated to ARCS on proposal num-

ber IPTS-31742.1 and HB-2A on proposal number IPTS-31409.1.

-
- [1] J. D. Reger and A. P. Young, Monte Carlo simulations of the spin-1/2 Heisenberg antiferromagnet on a square lattice, *Phys. Rev. B* **37**, 5978 (1988).
- [2] E. Dagotto and A. Moreo, Phase diagram of the frustrated spin-1/2 Heisenberg antiferromagnet in 2 dimensions, *Phys. Rev. Lett.* **63**, 2148 (1989).
- [3] M. S. Makivić and H.-Q. Ding, Two-dimensional spin-1/2 Heisenberg antiferromagnet: A quantum Monte Carlo study, *Phys. Rev. B* **43**, 3562 (1991).
- [4] H. J. Schulz and T. A. L. Ziman, Finite-size scaling for the two-dimensional frustrated quantum heisenberg antiferromagnet, *Europhysics Letters* **18**, 355 (1992).
- [5] P. Chandra and B. Douçot, Possible spin-liquid state at large S for the frustrated square Heisenberg lattice, *Phys. Rev. B* **38**, 9335 (1988).
- [6] H.-C. Jiang, H. Yao, and L. Balents, Spin liquid ground state of the spin- $\frac{1}{2}$ square J_1 - J_2 Heisenberg model, *Phys. Rev. B* **86**, 024424 (2012).
- [7] S. Morita, R. Kaneko, and M. Imada, Quantum spin liquid in spin 1/2 J_1 - J_2 Heisenberg model on square lattice: Many-variable variational Monte Carlo study combined with quantum-number projections, *Journal of the Physical Society of Japan* **84**, 024720 (2015), doi: 10.7566/JPSJ.84.024720.
- [8] S.-S. Gong, W. Zhu, D. N. Sheng, O. I. Motrunich, and M. P. A. Fisher, Plaquette ordered phase and quantum phase diagram in the spin- $\frac{1}{2}$ J_1 - J_2 square Heisenberg model, *Phys. Rev. Lett.* **113**, 027201 (2014).
- [9] W.-Y. Liu, S.-S. Gong, Y.-B. Li, D. Poilblanc, W.-Q. Chen, and Z.-C. Gu, Gapless quantum spin liquid and global phase diagram of the spin-1/2 $J_1 - J_2$ square antiferromagnetic Heisenberg model, *Science Bulletin* **67**, 1034 (2022).
- [10] Z. Zhu and S. R. White, Spin liquid phase of the $S = 1/2 J_1 - J_2$ heisenberg model on the triangular lattice, *Phys. Rev. B* **92**, 041105 (2015).
- [11] W.-J. Hu, S.-S. Gong, W. Zhu, and D. Sheng, Competing spin-liquid states in the spin-1/2 Heisenberg model on the triangular lattice, *Phys. Rev. B* **92**, 140403 (2015).
- [12] Y. Iqbal, W.-J. Hu, R. Thomale, D. Poilblanc, and F. Becca, Spin liquid nature in the Heisenberg J_1 - J_2 triangular antiferromagnet, *Phys. Rev. B* **93**, 144411 (2016).
- [13] Z. Zhu, P. Maksimov, S. R. White, and A. Chernyshev, Topography of spin liquids on a triangular lattice, *Phys. Rev. Lett.* **120**, 207203 (2018).
- [14] J. Xiang, C. Zhang, Y. Gao, W. Schmidt, K. Schmalzl, C.-W. Wang, B. Li, N. Xi, X.-Y. Liu, H. Jin, *et al.*, Giant magnetocaloric effect in spin supersolid candidate $\text{Na}_2\text{BaCo}(\text{PO}_4)_2$, *Nature* **625**, 270 (2024).
- [15] M. Zhu, V. Romerio, N. Steiger, S. D. Nabi, N. Murai, S. Ohira-Kawamura, K. Y. Povarov, Y. Skourski, R. Sibille, L. Keller, Z. Yan, S. Gvasaliya, and A. Zheleudev, Continuum excitations in a spin supersolid on a triangular lattice, *Phys. Rev. Lett.* **133**, 186704 (2024).
- [16] P. Park, E. A. Ghioldi, A. F. May, J. A. Kolopus, A. A. Podlesnyak, S. Calder, J. A. M. Paddison, A. E. Trumper, L. O. Manuel, C. D. Batista, M. B. Stone, G. B. Halász, and A. D. Christianson, Anomalous continuum scattering and higher-order van hove singularity in the strongly anisotropic $S=1/2$ triangular lattice antiferromagnet, *Nature Communications* **15**, 7264 (2024).
- [17] J. G. Rau, E. K.-H. Lee, and H.-Y. Kee, Generic spin model for the honeycomb iridates beyond the kitaev limit, *Phys. Rev. Lett.* **112**, 077204 (2014).
- [18] A. Banerjee, J. Yan, J. Knolle, C. A. Bridges, M. B. Stone, M. D. Lumsden, D. G. Mandrus, D. A. Tennant, R. Moessner, and S. E. Nagler, Neutron scattering in the proximate quantum spin liquid $\alpha - \text{RuCl}_3$, *Science* **356**, 1055 (2017).
- [19] H. Takagi, T. Takayama, G. Jackeli, G. Khaliullin, and S. E. Nagler, Concept and realization of kitaev quantum spin liquids, *Nature Reviews Physics* **1**, 264 (2019).
- [20] P. Maksimov, Z. Zhu, S. R. White, and A. Chernyshev, Anisotropic-exchange magnets on a triangular lattice: spin waves, accidental degeneracies, and dual spin liquids, *Phys. Rev. X* **9**, 021017 (2019).
- [21] C. Kim, S. Kim, P. Park, T. Kim, J. Jeong, S. Ohira-Kawamura, N. Murai, K. Nakajima, A. Chernyshev, M. Mourigal, *et al.*, Bond-dependent anisotropy and magnon decay in cobalt-based kitaev triangular antiferromagnet, *Nature Physics* **19**, 1624 (2023).
- [22] G. Jackeli and G. Khaliullin, Mott insulators in the strong spin-orbit coupling limit: From heisenberg to a quantum compass and kitaev models, *Phys. Rev. Lett.* **102**, 017205 (2009).
- [23] P. Park, G. Sala, T. Proffen, M. B. Stone, A. D. Christianson, and A. F. May, Quantum magnetism in the frustrated square lattice oxyhalides YbBi_2IO_4 and $\text{YbBi}_2\text{ClO}_4$, *Phys. Rev. B* **109**, 014426 (2024).
- [24] V. K. Singh, K. Nam, M. Barik, K. Boya, E. Kermarrec, P. Khuntia, K. H. Kim, S. Bhowal, and B. Koteswararao, $\text{Bi}_2\text{YbO}_4\text{Cl}$: A two-dimensional square-lattice compound with $J_{\text{eff}} = \frac{1}{2}$ magnetic moments, *Phys. Rev. B* **109**, 075128 (2024).
- [25] M. Schmidt, H. Oppermann, C. Hennig, R. W. Henn, E. Gmelin, N. Söger, and M. Binnewies, Untersuchungen zu bismutseltenerdoxidhalogeniden der zusammensetzung $\text{Bi}_2\text{REO}_4\text{X}$ ($\text{X} = \text{Cl}, \text{Br}, \text{I}$), *Zeitschrift für anorganische und allgemeine Chemie* **626**, 125 (2000).
- [26] J. c. v. Chaloupka, G. Jackeli, and G. Khaliullin, Kitaev-heisenberg model on a honeycomb lattice: Possible exotic phases in iridium oxides A_2IrO_3 , *Phys. Rev. Lett.* **105**, 027204 (2010).
- [27] J. G. Rau and M. J. P. Gingras, Frustration and anisotropic exchange in ytterbium magnets with edge-shared octahedra, *Phys. Rev. B* **98**, 054408 (2018).
- [28] Y. Motome, R. Sano, S. Jang, Y. Sugita, and Y. Kato, Materials design of kitaev spin liquids beyond the jackeli-khaliullin mechanism, *Journal of Physics: Condensed Matter* **32**, 404001 (2020).
- [29] S.-H. Jang, R. Sano, Y. Kato, and Y. Motome, Antiferromagnetic kitaev interaction in f -electron based honeycomb magnets, *Phys. Rev. B* **99**, 241106 (2019).

- [30] K. Momma and F. Izumi, *VESTA3* for three-dimensional visualization of crystal, volumetric and morphology data, *Journal of Applied Crystallography* **44**, 1272 (2011).
- [31] R. T. Azuah, L. R. Kneller, Y. Qiu, P. L. Tregenna-Piggott, C. M. Brown, J. R. Copley, and R. M. Dimeo, Dave: a comprehensive software suite for the reduction, visualization, and analysis of low energy neutron spectroscopic data, *Journal of research of the National Institute of Standards and Technology* **114**, 341 (2009).
- [32] O. Arnold, J.-C. Bilheux, J. Borreguero, A. Buts, S. I. Campbell, L. Chapon, M. Doucet, N. Draper, R. F. Leal, M. Gigg, *et al.*, Mantid—data analysis and visualization package for neutron scattering and μ sr experiments, *Nuclear instruments and methods in physics research section a: accelerators, spectrometers, detectors and associated equipment* **764**, 156 (2014).
- [33] J. Rodriguez-Carvajal, Recent advances in magnetic structure determination by neutron powder diffraction, *Physica B* **192**, 55 (1993).
- [34] A. Abragam and B. Bleaney, *Electron paramagnetic resonance of transition ions* (OUP Oxford, 2012).
- [35] A. Kutuzov and A. Skvortsova, Crystal electric field parameters for Yb³⁺ ion in YbRh₂Si₂, in *Journal of Physics: Conference Series*, Vol. 324 (IOP Publishing, 2011) p. 012039.
- [36] K. Stevens, Matrix elements and operator equivalents connected with the magnetic properties of rare earth ions, *Proceedings of the Physical Society. Section A* **65**, 209 (1952).
- [37] Q. Ma, X. Bai, E. Feng, G. Zhang, and H. Cao, *Crys-FieldExplorer*: rapid optimization of the crystal field Hamiltonian, *Journal of Applied Crystallography* **56**, 1229 (2023).
- [38] K. Lea, M. Leask, and W. Wolf, The raising of angular momentum degeneracy of f-electron terms by cubic crystal fields, *Journal of Physics and Chemistry of Solids* **23**, 1381 (1962).
- [39] O. Mustonen, S. Vasala, K. P. Schmidt, E. Sadrollahi, H. C. Walker, I. Terasaki, F. J. Litterst, E. Baggio-Saitovitch, and M. Karppinen, Tuning the $S = 1/2$ square-lattice antiferromagnet Sr₂Cu(Te_{1-x}W_x)O₆ from néel order to quantum disorder to columnar order, *Phys. Rev. B* **98**, 064411 (2018).
- [40] H. Ishikawa, N. Nakamura, M. Yoshida, M. Takigawa, P. Babkevich, N. Qureshi, H. M. Rønnow, T. Yajima, and Z. Hiroi, J_1 – J_2 square-lattice heisenberg antiferromagnets with $4d^1$ spins: AMoOPO₄Cl ($A = \text{K, Rb}$), *Phys. Rev. B* **95**, 064408 (2017).
- [41] A. Bombardi, J. Rodriguez-Carvajal, S. Di Matteo, F. de Bergevin, L. Paolasini, P. Carretta, P. Millet, and R. Caciuffo, Direct determination of the magnetic ground state in the square lattice $S = 1/2$ antiferromagnet Li₂VOSiO₄, *Phys. Rev. Lett.* **93**, 027202 (2004).
- [42] P. Park, G. Sala, D. M. Pajerowski, A. F. May, J. A. Kolopus, D. Dahlbom, M. B. Stone, G. B. Halász, and A. D. Christianson, Quantum and classical spin dynamics across temperature scales in the $S = 1/2$ heisenberg antiferromagnet, *Phys. Rev. Res.* **6**, 033184 (2024).
- [43] R. Bishop, P. Li, R. Darradi, J. Schulenburg, and J. Richter, Effect of anisotropy on the ground-state magnetic ordering of the spin-half quantum $J_1\text{XXZ} - J_2\text{XXZ}$ model on the square lattice, *Phys. Rev. B—Condensed Matter and Materials Physics* **78**, 054412 (2008).
- [44] R. F. Bishop, P. H. Y. Li, O. Götze, and J. Richter, Frustrated spin- $\frac{1}{2}$ heisenberg magnet on a square-lattice bilayer: High-order study of the quantum critical behavior of the J_1 – J_2 – J_1^\perp model, *Phys. Rev. B* **100**, 024401 (2019).
- [45] K. A. Ross, L. Savary, B. D. Gaulin, and L. Balents, Quantum excitations in quantum spin ice, *Phys. Rev. X* **1**, 021002 (2011).
- [46] S. Khatua, G. C. Howson, M. J. Gingras, and J. G. Rau, Ground state properties of the heisenberg-compass model on the square lattice, *Phys. Rev. B* **110**, 104426 (2024).
- [47] J. S. Gardner, M. J. Gingras, and J. E. Greedan, Magnetic pyrochlore oxides, *Reviews of Modern Physics* **82**, 53 (2010).
- [48] J. D. Thompson, P. A. McClarty, D. Prabhakaran, I. Cabrera, T. Guidi, and R. Coldea, Quasiparticle breakdown and spin hamiltonian of the frustrated quantum pyrochlore Yb₂Ti₂O₇ in a magnetic field, *Phys. Rev. Lett.* **119**, 057203 (2017).
- [49] J. G. Rau, R. Moessner, and P. A. McClarty, Magnon interactions in the frustrated pyrochlore ferromagnet Yb₂Ti₂O₇, *Phys. Rev. B* **100**, 104423 (2019).
- [50] C. Sarkis, J. G. Rau, L. Sanjeeva, M. Powell, J. Kollis, J. Marbey, S. Hill, J. Rodriguez-Rivera, H. Nair, D. Yahne, *et al.*, Unravelling competing microscopic interactions at a phase boundary: A single-crystal study of the metastable antiferromagnetic pyrochlore Yb₂Ge₂O₇, *Phys. Rev. B* **102**, 134418 (2020).

Appendix A: Assessing other potential solutions of the crystal field excitation analysis

Tables III and IV present the eigenvalues and eigenstates corresponding to the optimal crystal field parameters listed in Table II, specifically for the case of $B_0^2 = -0.1068$ meV for YbBi_2IO_4 . While the fitting result indicates a good agreement from a few other parameter sets for $\text{YbBi}_2\text{ClO}_4$, these alternative solution candidates, with $B_2^0 = -1.48$ and 1.06 meV [see Fig. 3(c)], do not accurately represent the magnetic properties of $\text{YbBi}_2\text{ClO}_4$. The complete parameter sets of these alternative solutions (in meV) are as follows:

$$\begin{aligned} B_0^2 &= 1.06, B_2^4 = -0.050, B_4^4 = -0.154, \\ B_0^6 &= 0.0026, B_4^6 = -0.0131, \end{aligned} \quad (\text{A1})$$

$$\begin{aligned} B_0^2 &= -1.48, B_2^4 = -0.043, B_4^4 = 0.174, \\ B_0^6 &= -0.0007, B_4^6 = 0.0214. \end{aligned} \quad (\text{A2})$$

Notably, both solutions yield a Γ_6^t doublet ground state, different from those given by the solutions presented in TABLE II. The corresponding g -factors are:

$$g_{ab} = 4.085, g_c = 0.170, \quad (\text{A3})$$

$$g_{ab} = 0.907, g_c = 6.185. \quad (\text{A4})$$

However, the average g -factors for these solutions, calculated as $g_{\text{avg}} = (2g_{ab} + g_c)/3$, are 2.780 and 2.666, respectively. These values are significantly smaller than

the g_{avg} value for $\text{YbBi}_2\text{ClO}_4$ obtained from Curie-Weiss fitting and saturated magnetization of the $M - H$ curve [23, 24]. On the other hand, the chosen solution in TABLE II giving a Γ_7^t ground state yields a correct g_{avg} .

Appendix B: Comparing octahedral and cubic ligand configurations

Here, we highlight some crucial similarities and differences between $J_{\text{eff}} = 1/2$ magnetism in the widely studied traditional octahedral ligand configuration and our case with a nearly cubic environment [27]. First, the doublet ground state found in YbBi_2IO_4 and $\text{YbBi}_2\text{ClO}_4$ (Table. II), which is not far from the perfect cubic case [Eq. (7)], falls into the same Γ_7 representation as the $J_{\text{eff}} = 1/2$ doublet realized in transition metal systems with octahedral ligand configurations (e.g., d^5 iridates and ruthenates, and d^7 cobaltates) [27, 28]. It is also noteworthy that $4f^1$ rare-earth systems with the octahedral environment (e.g., Ce^{3+}), which were suggested to exhibit strong antiferromagnetic Kitaev interactions, also configures the same Γ_7 ground state doublet as Γ_7^t in Eq. (3) [28]. Second, concerning the NN superexchange interactions, both configurations consist of two symmetry-equivalent exchange paths [see Fig. 1(b)]. On the other hand, a contrasting feature is the bond angle: unlike a 90° bond angle found in the octahedral configuration, the cubic configuration is characterized by a tetrahedral bond angle, $\cos^{-1}(-1/3) = 109.47^\circ$. Each aspect crucially influences the underlying hopping processes and the net exchange interaction matrix, thereby difficult to infer what would happen in the cubic case without explicit calculation of the hopping processes.

TABLE III. Eigenvalues and Eigenvectors of the Yb^{3+} crystal field levels in $\text{YbBi}_2\text{ClO}_4$

E (meV)	$ -\frac{7}{2}\rangle$	$ -\frac{5}{2}\rangle$	$ -\frac{3}{2}\rangle$	$ -\frac{1}{2}\rangle$	$ \frac{1}{2}\rangle$	$ \frac{3}{2}\rangle$	$ \frac{5}{2}\rangle$	$ \frac{7}{2}\rangle$
0.000	0.0	0.0	0.5804	0.0	0.0	0.0	-0.8143	0.0
0.000	0.0	0.8143	0.0	0.0	0.0	-0.5804	0.0	0.0
80.78	-0.9999	0.0	0.0	0.0	0.0080	0.0	0.0	0.0
80.78	0.0	0.0	0.0	0.0080	0.0	0.0	0.0	-0.9999
88.12	0.0	-0.5804	0.0	0.0	0.0	-0.8143	0.0	0.0
88.12	0.0	0.0	-0.8143	0.0	0.0	0.0	-0.5804	0.0
101.31	0.0	0.0	0.0	0.9999	0.0	0.0	0.0	0.0080
101.31	-0.0080	0.0	0.0	0.0	-0.9999	0.0	0.0	0.0

TABLE IV. Eigenvalues and Eigenvectors of the Yb^{3+} crystal field levels in YbBi_2IO_4

E (meV)	$ -\frac{7}{2}\rangle$	$ -\frac{5}{2}\rangle$	$ -\frac{3}{2}\rangle$	$ -\frac{1}{2}\rangle$	$ \frac{1}{2}\rangle$	$ \frac{3}{2}\rangle$	$ \frac{5}{2}\rangle$	$ \frac{7}{2}\rangle$
0.000	0.0	0.0	0.6194	0.0	0.0	0.0	-0.7851	0.0
0.000	0.0	0.7851	0.0	0.0	0.0	-0.6194	0.0	0.0
79.61	-0.9820	0.0	0.0	0.0	0.1890	0.0	0.0	0.0
79.61	0.0	0.0	0.0	0.1890	0.0	0.0	0.0	-0.9820
86.32	0.0	-0.6194	0.0	0.0	0.0	-0.7851	0.0	0.0
86.32	0.0	0.0	-0.7851	0.0	0.0	0.0	-0.6194	0.0
92.65	0.0	0.0	0.0	0.9820	0.0	0.0	0.0	0.1890
92.65	-0.1890	0.0	0.0	0.0	-0.9820	0.0	0.0	0.0